A&A 467, 207–216 (2007)
DOI: 10.1051/0004-6361:20065682

Astronomy & Astrophysics

Probing the initial conditions of high mass star formation

I. Deuteration and depletion in high mass pre/protocluster clumps⋆

T. Pillai[1,⋆⋆], F. Wyrowski[1], J. Hatchell[2], A. G. Gibb[3], and M. A. Thompson[4]

[1] Max-Planck-Institut für Radioastronomie, Auf dem Hügel 69, 53121 Bonn, Germany
e-mail: tpillai@cfa.harvard.edu
[2] School of Physics, University of Exeter, Stocker Road, Exeter EX4 4QL, UK
[3] Department of Physics & Astronomy, University of British Columbia, Vancouver, BC, V6T 1Z1, Canada
[4] Centre for Astrophysics Research, Science & Technology Research Institute, University of Hertfordshire, College Lane, Hatfield, AL10 9AB, UK

Received 23 May 2006 / Accepted 5 February 2007

ABSTRACT

Aims. UltraCompact HII regions are signposts of high-mass star formation. Since high-mass star formation occurs in clusters, one expects to find even earlier phases of massive star formation in the vicinity of UltraCompact HII regions. Here, we study the amount of deuteration and depletion toward pre/protocluster clumps found in a wide-field (10×10 arcmin) census of clouds in 32 massive star-forming regions that are known to harbour UCHII regions.

Methods. We determine the column density of NH_3, NH_2D, CO, $H^{13}CN$, and $HC^{15}N$ lines. We used the $(J, K) = (1, 1)$ and $(2, 2)$ inversion transitions of NH_3 to constrain the gas temperatures.

Results. We find that 65% of the observed sources have strong NH_2D emission and more than 50% of the sources exhibit a high degree of deuteration, ($0.1 \leq NH_2D/NH_3 \leq 0.7$), 0.7 being the highest observed deuteration of NH_3 reported to date. Our search for NHD_2 in two sources did not result in a detection. The enhancement in deuteration coincides with moderate CO depletion onto dust grains. There is no evidence of a correlation between the two processes, though an underlying correlation cannot be ruled out as the depletion factor is very likely to be only a lower limit. Based on simultaneously observed $H^{13}CN$ and $HC^{15}N$ ($J = 1$–0) lines, we derive a high abundance ratio of $H^{13}CN$ to $HC^{15}N$, which might indicate anomalous ratios of C and N isotopes relative to those derived toward the local ISM.

Conclusions. We find CO depletion and high deuteration towards cold cores in massive star forming regions. Therefore, these are good candidates for sources at the early phases of massive star formation. While our sensitive upper limits on NHD_2 do not prove the predictions of the gas-phase and grain chemistry models wrong, an enhancement of $\approx 10^4$ over the cosmic D/H ratio from NH_2D warrants explanation.

Key words. stars: formation – astrobiology – molecular data – methods: observational – ISM: clouds – radio lines: ISM

1. Introduction

The earliest phases of high mass star formation are still poorly understood. The prevalent theory is that massive stars are born in dense clumps within giant molecular clouds (GMCs), where the presence of UltraCompact HII regions (UCHII) identifies massive stars which have already begun to ionize their surroundings. Observations (Cesaroni et al. 1994, 1998) have shown that these are often associated with warm ($T > 100$ K), compact (<0.1 pc) and very dense ($n_{H_2} > 10^7$ cm^{-3}) cores known as hot molecular cores (HMCs). An evolutionary sequence has been suggested based on recent observations (Codella et al. 2004; Beuther & Shepherd 2005) with the HMC stage immediately preceding the formation of UCHII regions. But the stage before hot cores – the precluster and early protocluster phases of massive star formation – have not yet been studied. Since many UCHII regions are located in clusters, one expects to find even earlier phases of massive star formation, and the raw material out of which massive stars or star clusters form, in the vicinity of UCHIIs (Thompson et al. 2006).

This has prompted us to embark upon a program to search for massive pre/protocluster clumps by taking a wide-field (10×10 arcmin) census of clouds in 32 massive star-forming regions, harbouring UCHII regions (Wood & Churchwell 1989). Our program is known as SCAMPS (the SCUBA Massive Pre/Protocluster core Survey; Thompson et al. 2005; Thompson et al. 2007, in prep.).

We discovered a multitude of secondary, cold condensations and warmer clumps that might contain heavily embedded massive protostars. Many of the sources are seen as dark patches in MSX infrared images of the region, infrared dark clouds (IRDCs; Menten et al. 2005). As a result these clumps must have dust temperatures below 30 K (as evidenced by MIR upper limits) and have masses of a few 100 to 1000 $M_\odot$. These clumps thus could be in a colder pre-protostellar phase.

In order to study the physical and chemical conditions of these clumps, we carried out a multi-wavelength survey toward them in various molecular tracers. In this study, we also included 9 sources which were selected on the basis of the MIR extinction (IRDCs) and followed up later with submillimeter dust

⋆ Appendix A is only available in electronic form at http://www.aanda.org
⋆⋆ *Present address*: Harvard-Smithsonian Centre for Astrophysics.

continuum emission and millimeter rotational lines of H_2CO (Carey et al. 1998). We have recently reported a study of ammonia in this sample (Pillai et al. 2006). Here, we report on our study using ammonia to probe the temperature and deuteration in the clumps and CO to estimate depletion of neutral molecules from the gas phase. Depletion has proved to be a good tracer of low-mass pre-stellar cores (Bacmann et al. 2003 and Crapsi et al. 2005), and NH_3 is an important tool in measuring the physical conditions in molecular clouds and can be used to confirm the low temperatures and high densities required for depletion (Ho & Townes 1983). Since only the lowest NH_3 energy levels are expected to be populated for cold dark clouds ($T < 20$ K), their physical conditions can be probed using the (1, 1) and (2, 2) inversion transitions in the metastable (J, K) rotational levels of ammonia. Radiative transitions between different K-ladders are forbidden, therefore the lowest levels are populated only via collisions. The optical depth can be determined from the ratio of the hyperfine satellites. Thus, the population of the different levels can be estimated and hence the temperature of the gas determined.

NH_3 is observed to be an excellent tracer of the dense gas where many other molecules would have heavily depleted (Tafalla et al. 2004). In addition, recent chemical models reveal that NH_3 (and also N_2H^+), does not deplete from the gas phase for the densities observed in dark clouds ($<10^6$ cm^{-3}; Bergin & Langer 1997). However in the light of recent experiments of the desorption of CO and N_2 at temperatures relevant to dense cores, the relative difference between the derived CO and N_2 binding energies is found to be significantly less than that currently adopted in astrochemical models (Öberg et al. 2005). Therefore, the observed non-depletion of NH_3 and N_2H^+ during the early formation of a massive cluster remains a "mystery".

High densities in the earliest phase are expected to enhance depletion of molecules (mainly CO) onto grains (Bacmann et al. 2003). The freeze out of abundant gas phase molecules along with the low temperatures (≤20 K) prevalent in these clumps leads to a high degree of deuteration (Flower et al. 2005; Roueff et al. 2005; Hatchell 2003; Shah & Wootten 2001; Saito et al. 2000). Hence, the estimation of deuteration and depletion in clumps can be used as a chemical and physical chronometer.

In this paper we investigate the NH_3 temperature and deuteration in our candidate pre/protocluster cores using observations with the Effelsberg 100 m and IRAM 30 m telescopes. In Sect. 2, we describe our single dish observations. We also discuss the data reduction and present the derived physical parameters for different molecules. In Sect. 3, we show that candidate pre/protocluster clumps exhibit very high deuteration and depletion. The fractionation of NH_3 is compared with depletion of CO from the gas phase. The possible origin of deuterated species and the variation of deuteration with gas temperature is also discussed. HCN was also observed as part of the 30 m observations and we conclude the discussion with our interpretation of the HCN isotopic abundance with galactic distance.

2. Observations and results

In this section we present the results of single dish observations of NH_3, NH_2D, CO and HCN lines on a sample of 23 SCAMPS sources and 9 IRDCs. The brightest compact submm sources with no MIR counterpart were selected for these observations from our original catalogue of the SCUBA fields. The parameters of the molecular transitions covered, along with the observing setups are given in Table 1. In Table 2, we give the source list. The derived line parameters and the column densities are presented in Tables 3–6.

Table 1. Parameters of observed rotational transitions.

Species	Transition	E_l^a (K)	ν (MHz)
NH_3	$(J, K = 1, 1)$	22.70	23 694.496
NH_3	$(J, K = 2, 2)$	63.89	23 722.633
NH_2D (para)	1_{11}–1_{01}	16.55	85 926.3
NH_2D (ortho)	1_{11}–1_{01}	15.98	110 153.6
NHD_2 (ortho)	1_{10}–1_{01}	13.33	110 812.9
NHD_2 (para)	1_{10}–1_{01}	13.09	110 896.7
$C^{18}O$	$J = 1$–0	0.0	109 782.1734
$C^{18}O$	$J = 2$–1	5.27	219 560.3568
$C^{17}O$	$J = 2$–1	5.39	224 714.3850
$H^{13}CN$	$J = 1$–0, $F = 2$–1	0.0	86 340.184
$HC^{15}N$	$J = 1$–0	0.0	86 054.961

Note: ^{a} E_l is the lower energy level of the transition.

Table 2. Positions and velocities of the observed sources. IRDC positions are taken from Carey et al. (1998).

Source	RA(2000)	Dec(2000)	v_{LSR} [km s^{-1}]
SCAMPS			
G8.13+0.25	18:02:55.69	–21:47:46.7	19.4
G8.68-0.37	18:06:23.24	–21:37:14.1	35.2/38.1
G8.71-0.37	18:06:26.51	–21:35:46.6	38.1
G10.21-0.31	18:09:20.63	–20:15:04.5	12.8
G10.21-0.32	18:09:24.52	–20:15:41.4	12.8
G10.15-0.34	18:09:21.38	–20:19:32.8	12.8
G10.61-0.33	18:10:15.62	–19:54:46.6	74.0
G12.19-0.12	18:12:41.67	–18:25:19.8	27.6
G13.18+0.06	18:14:00.92	–17:28:41.2	51.6
G15.01-0.67	18:20:21.22	–16:12:42.2	26.2
G15.03-0.65	18:20:18.80	–16:11:22.6	26.2
G15.01-0.69	18:20:24.22	–16:13:22.8	26.2
G18.17-0.30	18:25:07.53	–13:14:32.7	54.9
G18.21-0.34	18:25:21.55	–13:13:39.5	54.9
G23.41-0.23	18:34:45.74	–08:34:21.2	104.2
G23.42-0.23	18:34:48.16	–08:33:56.1	104.2
G23.44-0.18	18:34:39.25	–08:31:36.2	104.2
G27.29+0.15	18:40:34.70	–04:57:18.1	26.0
G27.31+0.18	18:40:32.45	–04:55:03.8	26.0
G29.97-0.05	18:46:12.25	–02:39:05.9	100
G34.81-0.28	18:53:20.148	+01:28:31.5	59.0
G35.19-1.73	19:01:45.45	+01:13:21.5	42.4
G81.74+0.59	20:39:00.37	+42:24:36.6	–3.1
IRDCs			
G11.11-0.12 NH_3 P1	18:10:34.04	–19:21:49.0	29.2
G11.11-0.12 NH_3 P3	18:10:07.25	–19:27:28.0	29.2
G11.11-0.12 NH_3 P4	18:10:07.25	–19:28:49.0	29.2
G19.30+0.07 NH_3 P1	18:25:58.14	–12:04:4.9	26.3
G19.30+0.07 NH_3 P2	18:25:52.69	–12:04:44.9	26.3
G28.34+0.06 NH_3 P1	18:42:50.9	–04:03:13.9	78.4
G28.34+0.06 NH_3 P2	18:42:52.4	–03:59:53.9	78.4
G33.71-0.01	18:52:53.81	+00:41:06.4	104.2
G79.34+0.33	20:32:26.20	+40:19:40.9	0.1

2.1. IRAM 30 m observations

The NH_2D, $C^{18}O$, $H^{13}CN$ and $HC^{15}N$ observations were made at the IRAM 30 m telescope[1] on Pico Veleta in August 2003

[1] IRAM is an international institute for research in millimeter astronomy. IRAM is supported by INSU/CNRS (France), MPG (Germany) and IGN (Spain).

toward the 32 candidate pre/protocluster clumps given in Table 2. We performed 9 point maps with 10″ spacing around the peak to be able to compare, independently of the beam, lines at different frequencies. All line parameters listed are averaged over the map.

Individual positions were observed with an integration time of 2 minutes per position in the position switch mode. The receivers A100, B100, A230 and B230 were tuned to 86.13, 109.975, 219.56 and 231.32 GHz respectively.

The VESPA autocorrelator was used at the backend, with a spectral resolution of 40 kHz and 320 kHz at 100 and 230 GHz respectively. We had average summer weather conditions with a maximum system temperature of 248 K at 110 GHz. Towards selected sources we also have $C^{17}O$ (J = 2–1) and NHD_2 (1_{10}–1_{01}) observations. The half power beam width (*HPBW*) of the 30 m telescope is 22″ at 110 GHz and 11″ at 230 GHz. The main beam efficiency at these frequencies is 0.75 and 0.52, respectively.

2.2. Effelsberg 100 m observations

We observed the NH_3 (1, 1) and (2, 2) transitions with the Effelsberg 100 m telescope [2] in April 2004 for the 23 sources listed in Table 2. Two of the sources were re-observed because of baseline problems with the receiver. With the AK 8192 backend, we were able to observe the (1, 1), (2, 2), (3, 3) and (4, 4) transitions in both polarisations simultaneously using the *K*-band receiver. With 8 subunits of 10 MHz bandwidth, the resulting spectral resolution was ≈0.25 km s^{-1}. The beam at the NH_3 frequencies was 40″. The observations were performed in the frequency switching mode. Pointing was checked at hourly intervals by continuum scans on G10.62. We estimate the pointing to be accurate to within 6″. The pointing scans were used for the absolute flux calibration. The NH_3 observations toward the 9 IRDCs are reported in Pillai et al. (2006). Note that for G12.19-0.12 and G29.97-0.05 we report the observations carried out in October 2002 with a spectral resolution of ≈1 km s^{-1}.

2.3. Results of the NH_3 and NH_2D single dish observations

The ratio of the brightness temperatures of the NH_3 (1, 1) and (2, 2) transitions, along with the optical depth, can be used to estimate the rotational temperature. For temperatures <20 K, which are typical for cold dark clouds, the rotational temperature closely follows the gas kinetic temperature (Walmsley & Ungerechts 1983). Like NH_3, its isotopologue NH_2D also has hyperfines which allows the estimation of optical depth and hence the column density. Thus the fractionation ratio can be estimated assuming that NH_2D and NH_3 are co-spatial and hence have the same gas temperature.

Out of the 32 sources that were observed, NH_2D with hyperfines were detected in 22 sources with S/N ratio >5σ while we have a 100% NH_3 (1, 1) and (2, 2) detection. While we detected the (3, 3) lines in most of the sources, the (4, 4) lines were not detected. The fits to the hyperfines for NH_3 and NH_2D were done using CLASS methods NH_3 (1, 1) and HFS respectively (Forveille et al. 1989). The line parameters from the resultant fits are given[3] in Tables A.2 and A.3. For those sources with a high uncertainty in the NH_2D optical depth, the main line is fitted with a single Gaussian and the integrated intensity is quoted. The spectra are shown in Fig. A.1.

The basic physical parameters, namely the rotational temperature, the kinetic temperature and ammonia column density were derived using the standard formulation for NH_3 spectra (Bachiller et al. 1987). The expressions used to estimate the column densities from the radiative transfer equations for all other molecules including NH_2D are given in Appendix A. The deduced physical parameters are given in Table 3. The uncertainties given in brackets are formal errors obtained by a Gaussian error propagation. We have derived the NH_2D column density solely based on the ortho transition. We assume that the ortho and para transitions are in LTE.

For the few cases with significant detection of the para state we find that ratio of the integrated line intensity ($\int T_{\rm MB} {\rm d}v$) is approximately 3 consistent with a thermalised ortho to para ratio of 3.

For the column density determination of NH_2D, we have averaged over the 9 points of the map to compare to the NH_3 results. Essentially the resolution of the NH_2D observations has been degraded to that of the NH_3 observations. A caveat is that a map obtained with 10″ spacing at the IRAM 30 m does not completely sample the 40″ beam of the Effelsberg telescope. However, it is very unlikely that there is significant emission outside the beam of the Effelsberg telescope (i.e. its *FWHM*) because a)we find that the brightest peak is always at the center of the map, b) box averaging delivers a similar result to a 1 D Gaussian weighted average c) the peak dust emission positions have been chosen as the centre coordinates for these observations.

The rotational temperatures are in a range from 11 to 23 K, with ammonia column densities from 1 to 5×10^{15} cm^{-3}. We obtain [NH_2D/NH_3] ratios from 0.004–0.66. A deuteration factor of 66% in NH_3 is much larger than the largest reported value so far, ∼33% by Hatchell (2003). In 10 out of the 22 sources with NH_2D detection, we obtain abundance ratios ≤0.02 while the rest of the sources have a high degree of deuteration (≥13%). These 10 sources with low ratios show optically thin NH_2D emission.

In Fig. 1, the correlation between the velocities and line widths of the NH_2D and NH_3 emission is shown. Velocities and line widths are clearly different in some sources, with the NH_2D line widths being smaller in most cases. This could be either due to NH_2D and NH_3 tracing different regions or the slightly different beams at the two frequencies, in which case, clumping might contribute to a larger line width. It is interesting to note that the critical density of the reported NH_2D transition is a factor 47 higher than that of the corresponding NH_3 transition, assuming similar collisional rates. However, a more likely explanation is that NH_3 could be originating from the more disturbed protocluster environment, while NH_2D might be tracing the gas in precluster cores (Pillai et al. in prep.).

2.4. Results of the CO observations

The $C^{18}O$ (1–0) and (2–1) observations were performed simultaneously with NH_2D ($1_{1,1}$–$1_{0,1}$). Figure A.2 shows the spectra toward all sources. Note that there are secondary features in

[2] Based on observations with the 100 m telescope of the MPIfR (Max-Planck-Institut für Radioastronomie) at Effelsberg).

[3] Table A.2, available in electronic form, contains the following information. Column 1 lists the name of the source, Cols. 2 and 5 gives the NH_3 (1, 1) and (2, 2) main beam brightness temperature respectively, Col. 3 gives the (1, 1) line width, and Col. 4 lists the (1, 1) main group optical depth. In Table A.3 we list the sources observed in NH_2D, the integrated line intensity, *FWHM* of the line and the total optical depth from Cols. 1 to 4.

Table 3. NH_2D and NH_3 column densities, rotational temperature and fractionation.

Source	$T_{\rm rot}$ [a]	$N_{\rm NH_3}$ [b]	$N_{\rm NH_2D}$ [c]	$[NH_2D/NH_3]$[d]
	K	$10^{15}\left(10^{14}\right)$ cm^{-2}	10^{13} cm^{-2}	
G8.13+0.25	18.0 (3.0)	1.8 (0.4)	1.7 (0.1)	1.0 (0.2)
	17.4 (2.3)	1.6 (0.3)	2.4 (0.1)	1.5 (0.3)
G8.68-0.37	12.1 (0.8)	1.3 (0.1)	39.4 (12.4)	30.3 (9.8)
G8.71-0.37	13.3 (1.0)	1.5 (0.2)	59.7 (10.6)	39.8 (8.9)
G10.21-0.31	15.4 (1.5)	2.1 (0.3)	70.9 (29.9)	33.7 (15.0)
G10.21-0.32	14.1 (0.7)	2.1 (0.1)	51.3 (22.3)	24.4 (10.7)
G10.61-0.33	17.8 (1.5)	2.3 (0.2)	1.0 (0.1)	0.4 (0.1)
G11.11-0.12P1	12.5 (1.2)	1.4 (0.2)	54.0 (23.5)	38.6 (17.7)
G11.11-0.12P4	10.6 (1.6)	1.8 (0.5)	1.7 (0.3)	0.9 (0.3)
G12.19-0.12	12.6 (0.3)	4.4 (0.2)	5.6 (0.2)	1.3 (0.1)
G13.18+0.06	17.4 (1.3)	2.8 (0.2)	88.9 (23.2)	31.7 (8.6)
G18.17-0.30	15.8 (1.2)	1.8 (0.2)	119.7 (31.5)	66.5 (19.0)
G18.21-0.34	15.5 (1.2)	1.7 (0.2)	47.3 (19.7)	27.8 (12.0)
G23.41-0.23	18.8 (1.8)	2.5 (0.3)	77.7 (51.3)	31.1 (20.8)
G23.44-0.18	23.3 (1.5)	5.2 (0.4)	5.0 (0.2)	1.0 (0.1)
G27.29+0.15	17.8 (1.7)	3.0 (0.3)	1.4 (0.2)	0.5 (0.1)
G28.34+0.06P2	15.7 (2.0)	2.2 (0.3)	4.1 (0.2)	1.9 (0.3)
G29.97-0.05	13.7 (1.4)	2.2 (0.3)	67.7 (15.2)	30.8 (8.1)
G33.71-0.01	19.5 (4.6)	3.0 (0.8)	1.4 (0.1)	0.5 (0.1)
G34.81-0.28	16.6 (1.0)	1.6 (0.1)	2.7 (0.2)	1.7 (0.2)
G35.19-1.73	17.0 (0.9)	1.8 (0.1)	74.0 (11.0)	41.1 (6.5)
G79.34+0.33	13.7 (1.0)	1.4 (0.1)	17.9 (15.9)	12.8 (11.4)
G81.74+0.59	18.4 (1.1)	2.7 (0.2)	92.9 (17.6)	34.4 (7.0)

[a] Rotational temperature derived from NH_3 observations. [b] NH_3 column density. [c] NH_2D column density. [d] Ratio of NH_3 and NH_2D column densities in percentage. Note: similar notations are used for other molecules elsewhere in this paper.

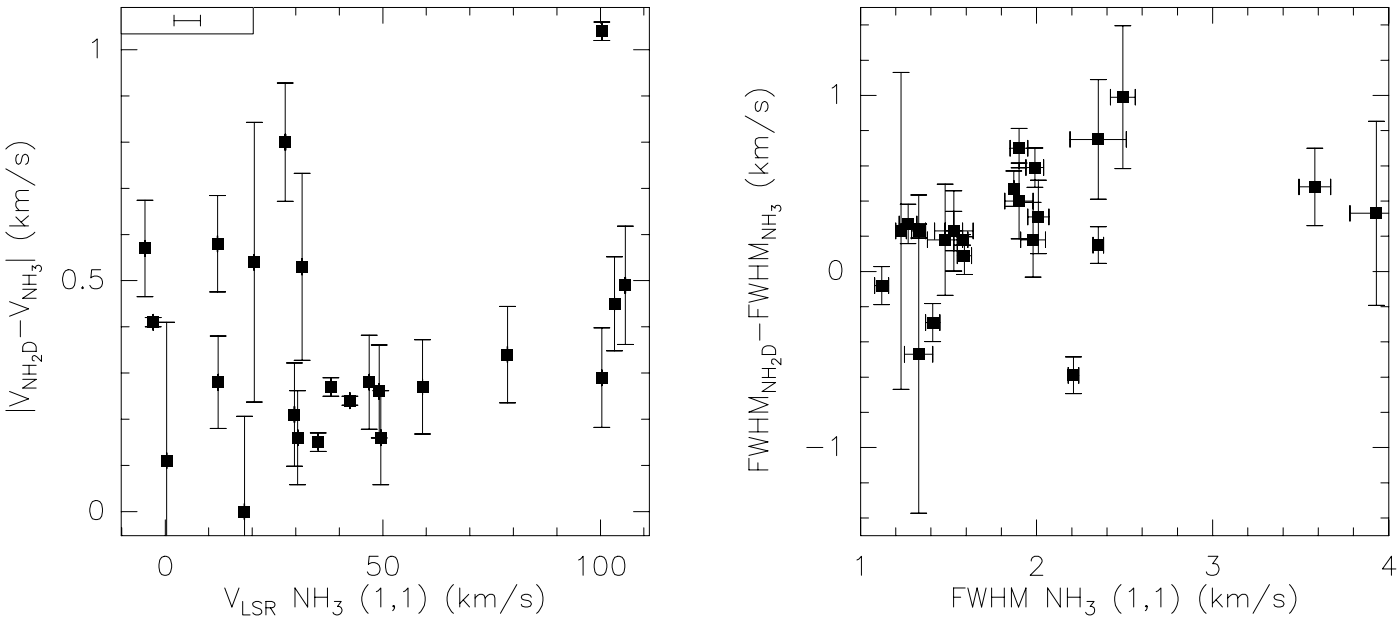

Fig. 1. *Left panel*: comparison of the LSR velocities of NH_3 and NH_2D. The median spectral resolution after Hanning smoothing is marked in the upper left corner of the panel. *Right panel*: comparison of NH_3 and NH_2D line widths. Points with no y error bars are those for which the line width has been fixed based on the hfs fit to the optically thin emission, to derive the NH_2D integrated intensity.

the $C^{18}O$ spectra for a few sources, likely to be line of sight components not seen in dense gas like NH_3. In Table A.4[4], we list the observed line parameters based on Gaussian fits, and, in Table 4, the column density and excitation temperature estimates (see Appendix A) and the $C^{18}O$ abundances. The $C^{18}O$ excitation temperature has been derived from the $C^{18}O$ J = 1–0 and J = 2–1 line ratios.

Based on the dust continuum and CO observations for the observed sample, the depletion can be studied for the first time on a sample of massive clumps. Recent observational studies on the condensation of CO in low mass prestellar cores reveal that in the initial cold and dense evolutionary stage, CO is heavily

[4] Table A.4, available in electronic form, contains the following information. Column 1 lists the name of the source, Cols. 2 and 3 gives the $C^{18}O$ (1–0) and (2–1) integrated intensity.

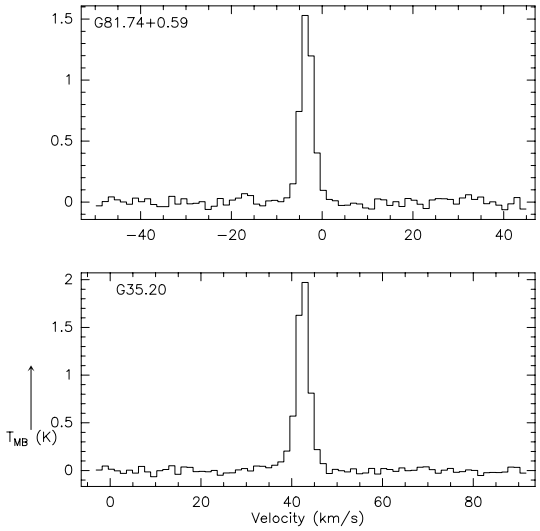

Fig. 2. $C^{17}O$ (J = 2–1) spectra toward G35.19-1.73 and G81.74+0.59 observed with the IRAM 30 m telescope.

depleted onto the dust grains (Bacmann et al. 2002, Savva et al. 2003). The depletion factor η is defined as

$$\eta \cdot \frac{N_{C^{18}O}}{[N_{H_2}]_{\rm observed}} = \frac{N_{C^{18}O}}{[N_{H_2}]_{\rm canonical}} \quad . \tag{1}$$

The $C^{18}O$ column density, $N_{C^{18}O}$, is derived from the observed integrated intensity (see Appendix A) and assumimg that the gas temperature is equal to the excitation temperature derived from the $C^{18}O$ line ratios.

The effective H_2 column density (Launhardt 1996) is calculated from

$$N(H_2) = \frac{6.2 \times 10^{16} S_\nu \lambda^3 \, e^{\frac{1.44\times10^4}{T_d \lambda}}}{\kappa_m(\lambda)\theta^2} \frac{Z_\odot}{Z} \tag{2}$$

where S_ν is the flux density in Jy/beam. λ the wavelength in μm, $Z/Z_\odot$ is the metalicity relative to the solar metalicity (we assume 1) and θ is the *FWHM* of the beam at wavelength λ. We used an opacity κ_m of 1.85 cm^2/g of dust at 850 μm for dust grains with thick ice mantles and gas density n(H) = 10^6 cm^{-3} (Ossenkopf & Henning 1994). The column density was derived after smoothing the 850 μm dust continuum emission to the 20″ resolution of the $C^{18}O$ data (Thompson et al. 2007, in prep).

In these dense clumps it is possible that the $C^{18}O$ line may be optically thick and hence derived column densities could be a lower limit. In order to investigate this possibility, we observed the rarer isotopomer $C^{17}O$ toward two of our sources, G35.19-1.73 and G81.74+0.59 as shown in Fig. 2. The line parameters are given in Table 5. In Sect. 3.1.1, we discuss how $C^{17}O$ is used as a more reliable tracer of the optical depth.

2.5. Results of the $H^{13}CN$ and $HC^{15}N$ observations

We also observed the isotopomeric species of HCN, $H^{13}CN$ and $HC^{15}N$ in our 3 mm setup with the IRAM 30 m telescope. $H^{13}CN$ was detected in almost all sources except G19.30P1/P2 and G10.15-0.34. In Fig. A.3, we show the spectra toward all sources where both $H^{13}CN$ and $HC^{15}N$ are detected with sufficient S/N ($\geq 3\sigma$). The $H^{13}CN$ line has hyperfines, which allows to estimate the optical depth. However, we find that $H^{13}CN$ is optically thin in almost all cases. In two sources with moderate optical depths, the uncertainty in τ is too large to derive meaningful constraints on the column density. The line parameters are given in Table 6 along with their column densities. The column density is computed using the gas temperature derived from NH_3 as the excitation temperature (see Appendix A).

3. Analysis and discussion

3.1. CO depletion

The derived $C^{18}O$ abundances are a factor of 2–12 lower than the canonical value of 1.7×10^{-7} (Frerking et al. 1982). Wu & Yang (2005) find similar depletion factors for the infrared dark cloud G79.2+0.38, another of the clumps in the cloud in the present study.

3.1.1. Is C^{18} optically thin?

As mentioned in Sect. 2.4, the CO column density as determined from $C^{18}O$ transitions might be underestimated if $C^{18}O$ is optically thick. However, the rarer isotopomer $C^{17}O$ is expected to be optically thin. The canonical value of the relative abundance of $C^{18}O$ w.r.t $C^{17}O$, $A(18, 17)$, is 3.65 (Wilson & Rood 1994) in the ISM. As discussed in Kramer et al. (1999), the measured ratios of the integrated intensities of the $C^{18}O$ and $C^{17}O$ lines can then be used to determine the $C^{18}O$ optical depth.

Due to the limited observing time, we observed the $C^{17}O$ line only in the two brightest $C^{18}O$ sources. If $R^{18,17}$ and $\tau_{18}^{18,17}$ denotes the ratio of the integrated intensities of the $C^{18}O$ and $C^{17}O$ lines and the optical depth of $C^{18}O$ as derived from the ratio, then

$$R^{18,17} = \frac{1 - \exp\left(-\tau_{18}^{18,17}\right)}{1 - \exp\left(-\tau_{18}^{18,17}/A(18,17)\right)}. \tag{3}$$

The assumptions involved in deriving Eq. (3), are that both isotopomers have the same excitation temperatures and beam filling factors.

For G35.19-1.73, we find that $\tau_{18}^{18,17} = 1.35$, which implies that the correction factor for the column density given by $\tau/(1 - \exp(-\tau)) = 1.8$, is clearly smaller than the observed depletion. However, for G81.74+0.59, the ratio itself $R^{18,17} \sim 6$, suggesting that Eq. (3) is not valid anymore. It is unlikely to be due to different excitation conditions or the extent of emission of $C^{18}O$ and $C^{17}O$. It is indeed possible that there are real variations in the ratio of ^{18}O to ^{17}O, a possibility which needs to be investigated. Additionally, the observed relatively small observed peak brightness temperatures for $C^{18}O$ exclude high optical depth in this line. Therefore, to the extent that we assume G35.19-1.73 to be representative of our sample, we may conclude that $C^{18}O$ optically depth is "moderate".

3.2. NH_3 deuteration

How do we account for the high deuteration we observe in these pre/protostellar clumps? There are two main pathways to bring about deuteration (Rodgers & Charnley 2001; Millar 2002, 2003; Roueff et al. 2005); a) gas-phase reactions, b) production of deuterium bearing molecules on grain surfaces. Accretion of neutrals onto the dust grains that would otherwise destroy H_2D^+ enhances deuteration. Up to now all these processes have been used to explain fractionation in different sources.

In pre/protostellar cores, ion-molecule exchange reactions prevalent at low temperatures coupled with the depletion of CO

Table 4. $C^{18}O$ column density and abundance from (J = 1–0) and (J = 2–1) transitions.

Source	T_{ex}	$N_{C^{18}O}$	$N(H_2)^a$	$\chi^b_{C^{18}O}$	η^c
	K	$10^{16}(10^{15})$ cm^{-2}	10^{23} cm^{-2}	10^{-8}	
G8.13+0.25	11.8	1.6 (0.1)	2.6	6.2	2.7
G8.68-0.37	8.5	2.4 (0.9)	7.9	3.0	5.6
G8.71-0.37	4.2	1.8 (0.5)	3.5	5.2	3.2
G10.15-0.34	19.1	2.1 (0.4)	3.8	5.4	3.1
G10.21-0.31	8.4	1.4 (0.2)	2.2	6.4	2.7
G10.21-0.32	8.0	2.6 (0.3)	7.4	3.6	4.8
G10.61-0.33	9.1	1.0 (0.3)	2.7	3.8	4.5
G11.11-0.12P1	6.4	0.6 (0.1)	1.1	5.5	3.1
G11.11-0.12P3	6.9	0.5 (0.3)	0.8	6.2	2.7
G11.11-0.12P4	6.6	0.5 (0.2)	1.4	3.5	4.8
G12.19-0.12	11.6	1.2 (0.2)	2.4	5.1	3.3
G13.18+0.06	15.7	1.2 (0.6)	6.3	1.8	9.3
G15.01-0.67	32.5	6.0 (0.4)	16.6	3.6	4.7
G15.01-0.69	52.2	4.5 (0.6)	11.6	3.9	4.4
G15.03-0.65	51.7	5.5 (0.6)	14.2	3.9	4.4
G18.17-0.30	14.3	1.5 (0.8)	3.3	4.6	3.7
G18.21-0.34	10.9	0.7 (0.4)	2.5	3.0	5.8
G23.41-0.23	8.4	3.4 (0.8)	9.3	3.6	4.7
G23.42-0.23	9.0	3.1 (0.3)	3.8	8.0	2.1
G23.44-0.18	9.2	3.0 (0.5)	7.7	3.9	4.3
G27.29+0.15	8.8	1.2 (0.2)	1.7	6.9	2.5
G27.31+0.18	8.3	0.5 (0.2)	1.7	2.7	6.3
G28.34+0.06P1	4.8	1.3 (0.5)	1.5	8.6	2.0
G28.34+0.06P2	8.7	1.4 (0.5)	7.8	1.8	9.6
G29.97-0.05	9.3	1.3 (0.7)	2.6	4.8	3.5
G79.34+0.33	8.4	0.7 (0.1)	2.1	3.5	4.9
G81.74+0.59	16.0	1.8 (0.2)	4.7	3.8	4.4

[a] H_2 column density derived from the 850 μm dust continuum flux measured using SCUBA. The dust temperature is assumed to be equal to the gas temperature derived from NH_3 (1, 1) and (2, 2) measurements as given in Table 3. [b] abundance of $C^{18}O$ relative to H_2. [c] depletion factor compared to the canonical value of $1.7{\cdot}10^{-7}$ (Frerking et al. 1982).

Table 5. $C^{17}O$ (J = 2–1) line parameters.

Source	$\int T_{MB} dv$	Δv
	K km s^{-1}	km s^{-1}
G35.19-1.73	7.1 (0.1)	3.3 (0.1)
G81.74+0.59	5.5 (0.1)	3.3 (0.1)

from gas phase is preferred over grain production of highly deuterated species at temperatures of 20 K (Shah & Wootten 2001; Caselli et al. 2003). The freeze-out of molecules from the gas onto the dust grains, particularly that of heavy molecules like CO in the cold initial phase has been predicted by chemical models (Flower et al. 2005; Rodgers & Charnley 2001; Roberts & Millar 2000a,b; Brown & Millar 1989b; Watson 1976). These predictions have been validated by observations of molecular freeze out onto dust grains in low-mass starless dense cores (Caselli et al. 1999; Tafalla et al. 2002). The primary fractionation reaction that dominates at low temperatures (<20 K) is

$$H_3^+ + HD \rightarrow H_2D^+ + H_2 + \Delta E_1. \quad (4)$$

Neutral molecules like CO can destroy H_2D^+, thereby lowering the deuterium enhancement. Therefore, the depletion of CO, the second most abundant molecule, from the gas phase can lead to an enhancement in the $[H_2D^+]/[H_3^+]$ ratio and thereby the molecular D/H ratios.

Roberts & Millar (2000b) show that at 10 K, accretion of neutrals onto the dust grains, especially CO, leads to the formation of doubly deuterated molecules such as NHD_2 and D_2CO. Based on these arguments, we expect to see a correlation between deuteration and CO depletion. In Fig. 3, we compare the NH_3 fractionation and the degree of CO depletion (depletion factor). As seen from the correlation plot, there is a large scatter in the values and we do not see any obvious trend of high depletion and deuteration. Nevertheless, the main result is that we find very high deuterium fractionation and CO depletion.

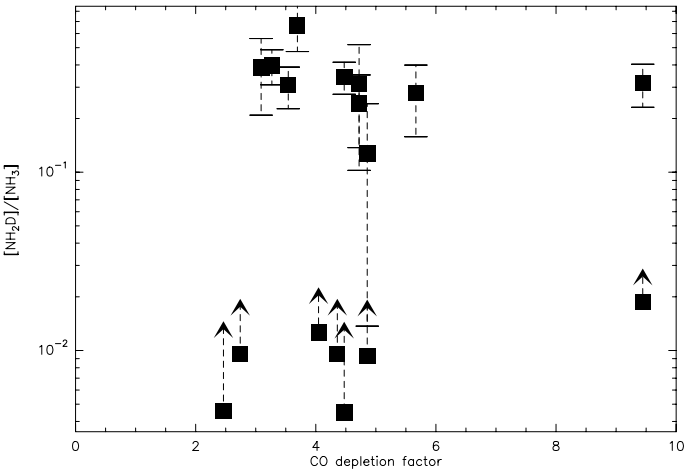

Fig. 3. Comparison of NH_3 fractionation and CO depletion factor for the dense clumps in our sample. The error bar on CO depletion factor is quite large mainly due to the uncertain dust opacities adopted (see Sect. 3.1).

Table 6. $H^{13}CN$ and $HC^{15}N$ line parameters and column density.

Source	$H^{13}CN$ J = 1–0, F = 2–1				$HC^{15}N$ J = 1–0		
	$\int T_{MB} dv^a$	Δv	T_{rot}	$N_{H^{13}CN}$	$\int T_{MB} dv$	Δv	$N_{HC^{15}N}$
	K km s^{-1}	km s^{-1}	K	10^{12} cm^{-2}	K km s^{-1}	km s^{-1}	10^{12} cm^{-2}
G10.21-0.31	0.9 (0.1)	3.5	15.4 (1.5)	12.2 (1.1)	0.2 (<0.1)	1.2 (0.4)	0.5 (0.1)
G10.21-0.32	0.7 (0.1)	2.4	14.5 (1.7)	9.3 (1.0)	0.6 (0.2)	5.6 (2.2)	1.3 (0.6)
G13.18+0.06	3.0 (0.1)	3.7	17.4 (1.3)	42.7 (2.5)	0.7 (0.1)	3.3 (0.4)	1.9 (0.2)
G15.01-0.67	7.3 (0.2)	3.4	24.3 (1.5)	129.5 (7.1)	2.6 (0.2)	2.8 (0.3)	8.6 (0.9)
G15.01-0.69	4.8 (0.2)	2.7	24.3 (1.3)	85.2 (4.3)	1.6 (0.1)	2.4 (0.2)	5.3 (0.4)
G15.03-0.65	3.6 (0.1)	3.6	20.4 (2.4)	55.9 (4.9)	1.3 (0.1)	3.6 (0.0)	4.4 (1.0)
	1.6 (0.1)	1.7	16.6 (2.9)	21.6 (2.6)	0.3 (0.1)	1.7 (0.0)	0.9 (0.2)
G23.41-0.23	1.3 (0.1)	2.0	18.8 (1.8)	18.6 (1.4)	0.5 (0.1)	2.6 (0.5)	1.3 (0.2)
G23.42-0.23	1.4 (0.1)	3.4	19.0 (2.0)	20.3 (1.7)	0.4 (0.1)	2.6 (0.4)	1.1 (0.2)
G28.34+0.06P2	1.0 (0.1)	2.4	15.7 (2.0)	13.8 (1.2)	0.7 (0.1)	3.7 (0.5)	1.8 (0.2)
G35.19-1.73	1.9 (0.1)	2.4	17.0 (0.9)	27.1 (1.3)	0.6 (0.1)	2.0 (0.3)	1.4 (0.2)
G79.34+0.33	0.8 (<0.1)	1.5	13.7 (1.0)	10.0 (0.5)	0.2 (<0.1)	1.2 (0.2)	0.5 (0.1)
G81.74+0.59	3.2 (0.1)	2.8	18.4 (1.1)	46.7 (2.3)	1.1 (0.1)	2.8 (0.2)	3.0 (0.2)

[a] Integrated line intensity for the $H^{13}CN$ main group alone.

Depletion could well occur on scales much smaller than the beam for sources at the distances typical for these sources (several kpc). In that case, the CO depletion that is measured as an average over the telescope beam is an underestimate of the true depletion. The NH_2D emission, on the other hand, is probably dominated by the dense clumps. This could explain why the CO depletion does not appear to track the deuteration in Fig. 3. The uncertainties on the CO depletion factors are quite large, mainly due to the uncertainty in the H_2 column density estimate from the 850 μm dust continuum. The largest uncertainty is a factor of 4 in the dust opacity at 850 μm (Ossenkopf & Henning 1994; Krügel & Siebenmorgen 1994; Draine & Lee 1984). But we note that with the choice of the Ossenkopf & Henning opacities, the derived column densities are already lower than for e.g. Savage & Mathis (1979) dust properties. The two studies other than ours that directly compare CO depletion and deuterium fraction are by Bacmann et al. (2003) and Crapsi et al. (2005). Bacmann et al. use the D_2CO to H_2CO ratios to determine the deuteration. They claim to find a correlation between D_2CO to H_2CO ratios and depletion and argue that the presence of a significant amount of O (which is also an important H_3^+ destroyer) in the gas phase still undepleted might be responsible for the large scatter observed. Crapsi et al. observe N_2H^+ and N_2D^+ toward 31 low-mass starless cores and find a good correlation between deuterium fractionation and CO depletion.

If f(X) is the fractional abundance of species X relative to H_2 and R(XD) is the abundance ratio of XD relative to XH, then under the assumption of steady-state and equating formation and destruction in Eq. (4), one finds (Millar 2003)

$$R(H_2D^+) = S_{H_2D^+}(T) f(HD). \quad (5)$$

where $S_{H_2D^+}(T)$ is a function of the different rate coefficients. (forward, backward and dissociative recombination rates) given by

$$S_{H_2D^+}(T) = \frac{k_{1f}}{k_{1r} + \alpha_1 f(e) + \Sigma k_M f(M)}. \quad (6)$$

Here, k_{1f}, k_{1r} are the forward and reverse rate coefficients such that $k_{1r} = k_{1f} \exp(-\Delta E_1/T)$ and $\alpha_1 \propto 1/\sqrt{T}$ is the dissociative recombination rate, f(e) is the electron fraction and Σk_M is the rate coefficient of H_2D^+ with species M. ΔE_1 is the exothermal energy (~220 K), also given in Eq. (4).

At low temperatures (T < 20 K) observed in cold cores, the primary fractionation reaction is dominated by the forward reaction in Eq. (4). At higher temperatures, the reverse reaction becomes important in removing H_2D^+ very rapidly from the gas phase. Consequently, the decrease in primary fractionation produces a corresponding decrease in secondary fractionation reactions responsible for deuterium enhancements in molecules. Therefore, one naively expects to find an anti-correlation between temperature and deuterium fractionation. In Fig. 4, we plot the NH_3 fractionation against the temperature for the high mass candidate pre/protostellar clumps (this paper) and for pre/protostellar clumps in the lower mass regime from the literature. The latest gas-phase predictions for $[NH_2D]/[NH_3]$ (Roueff et al. 2005) are also plotted. This model assumes a density of $n(H_2) = 10^5$ cm^{-3}, carbon and oxygen depletion factors of 5 and 15 respectively while Nitrogen is kept constant. Our data points nicely fill in the missing observed data points between 10–20 K. Clearly the agreement with the model is moderate.

The levels of deuteration do fall off rapidly with increasing temperature above 25 K (Roueff et al. 2005), but at the low temperatures shown here the dependence is small. The Roueff et al. models employ fixed H_2 densities of around 10^5 cm^{-3}, which would be typical averages over the 40″ beam for our sources. However the NH_2D emission will be enhanced at the peaks, where higher densities and higher depletion would be expected to produce higher levels of deuteration. Depletion, which increases over time roughly with the increase in density, has a strong influence on deuteration. The final levels of depletion and deuteration depend on the accretion history (e.g. Flower et al. 2005), but it is clear that higher densities or longer timescales result in higher levels of both, e.g. Roberts et al. (2003) derive $[NH_2D]/[NH_3]$ ratios of 0.4–0.8 for densities of 3×10^6 cm^{-3}.

However, most of the low $[NH_2D]/[NH_3]$ ratios and interestingly the high temperatures are from the sources where NH_2D column densities were estimated from the integrated intensity of the line and therefore are really lower limits on the $[NH_2D]/[NH_3]$ ratios. The exact temperature which we measure for a clump of course depends on the combination of hot/cold gas in the beam, which can explain the scatter between 15–18 K where in some cases we are still seeing a lot of deuteration and in others it has already diminished.

On average, the fractionation observed in sources in our sample is very high. However, note that few sources at temperatures

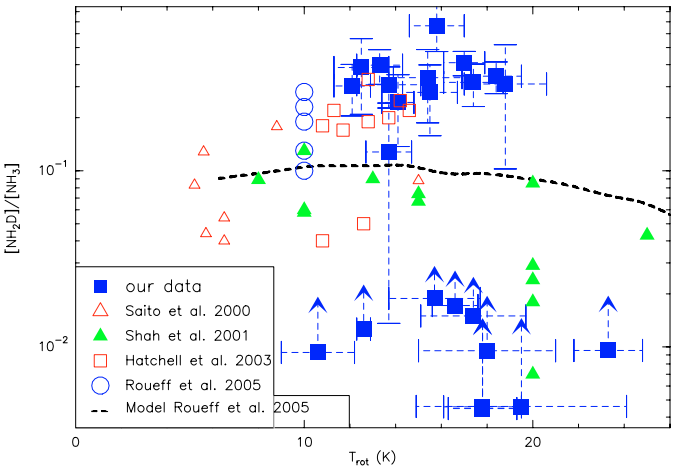

Fig. 4. Plot of NH_3 fractionation versus gas temperature as derived from NH_3. The dashed line is the latest gas phase model predictions (Roueff et al. 2005). The filled and unfilled squares mark the SCAMPS sources and Hatchell (2003) respectively; filled and unfilled triangles, the values found toward low mass pre/protostellar cores by Shah & Wootten (2001) and Saito et al. (2000) respectively and the unfilled circles mark Roueff et al. (2005) sources.

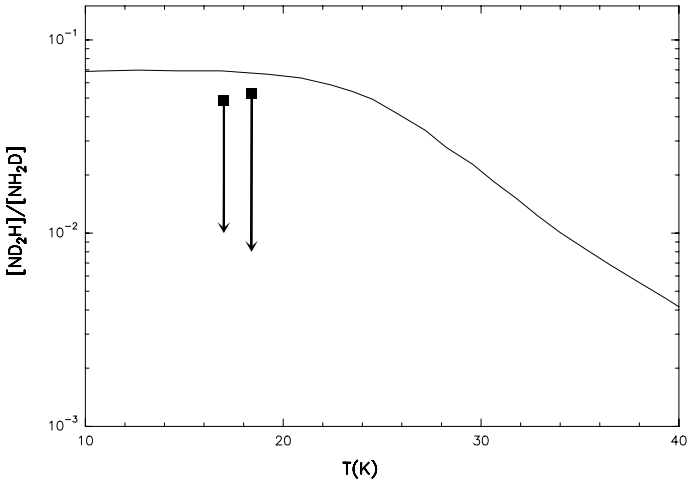

Fig. 5. Comparison of obtained upper limits for G35.19-1.73 and G81.74+0.59 with the gas phase model predictions (Roueff et al. 2005, their model 2).

above 15 K show an order of magnitude lower deuteration than the model predictions, while others show extremely high deuterations, much higher than those found in low mass pre/protostellar cores.

There could be three main reasons for the very low fractionation estimated for a few sources. First, one of the main assumption in deriving the $[NH_3]/[NH_2D]$ ratio is that the filling factors for both molecular transitions are the same. Any deviation from this assumption might result in a discrepant ratio. Second, these sources might be relatively more evolved. In such a case, the kinetic temperatures derived from the NH_3 (1, 1) and (2, 2) lines might only be a lower limit. In such cases where the gas temperature is roughly higher than 20 K, the rotational temperature does not represent the real gas temperature. Hence the column density (deuteration) determined may be under estimated. Third, the sources could be chemically young, hence the timescale to reach the high deuteration in these sources is larger than their age. Tafalla & Santiago (2004) recently discussed such a chemically young low mass core. It is also possible that NH_2D might be tracing different regions from NH_3 and that the temperature derived from NH_3 may not be the temperature of NH_2D.

3.2.1. Upper limits from NHD_2

A simple model for grain surface formation of multiply deuterated molecules is considered by Brown & Millar (1989a) and predicts the abundances of deuterated species, in order to differentiate between the gas and grain chemistry. According to the Brown and Millar model prediction, the abundances of deuterated species scale as $[NHD_2]/[NH_3] = \frac{1}{3}([NH_2D]/[NH_3])^2$ for grain surface formation.

Alternatively, Roberts & Millar (2000a) propose a gas-phase chemistry where the effects of the freeze out of gas phase species onto grains is included and find an enhancement in the fractionation of both singly and doubly deuterated species.

Very deep observations of the NHD_2 1_{10}–1_{01} line for two sources G35.19-1.73 and G81.74+0.59, did not result in any detection at an rms of ≈20 mK. Based on the 3σ upper limits, we then derive $[NHD_2]/[NH_3]$ (see Appendix A) and find that

$$([NHD_2]/[NH_3])_{\rm observed} < (0.02)_{\rm G35.19}; (0.02)_{\rm G81.74}$$

$$\left(\frac{1}{3}([NH_2D]/[NH_3])^2\right)_{\rm observed} < (0.06)_{\rm G35.19}; (0.04)_{\rm G81.74}$$

$$([NHD_2]/[NH_2D])_{\rm observed} < (0.05)_{\rm G35.19}; (0.05)_{\rm G81.74}.$$

The grain-chemistry model prediction is based purely on probability arguments assuming that the fractionation is proportional to gas-phase atomic D/H ratio and that there are three different pathways for inserting the D atom into the chain of reactions that form multiply deuterated NH_3. In spite of the simplicity of the model, the prediction is close to the derived upper limits in both sources.

How do the obtained upper limits compare with the predictions of recent gas-phase deuterium chemistry models? In Fig. 5, we compare the results of model calculations with our observed upper limits for the ratio of NHD_2 to NH_2D (Roueff et al. 2005). We have used their "model 2" which gives the highest molecular fractional abundances for the N-bearing species. In this context it is also interesting to note that while Roueff et al. find that their model underpredicts the NHD_2 to NH_2D ratio in low mass prestellar cores (LDN 134N, LDN 1689N, Barnard 1, LDN 1544), it agrees well with the observed ratio in our sample.

Hence, we cannot reject active grain or gas-phase chemistry on the basis of the observed NHD_2 upper limits. While a gas-phase model along with condensation of neutral species onto grain mantles adequately explains moderate deuteration (NH_2D/NH_3) observed towards some sources, the very high fractionation we derive remains unexplained. Although we do not understand the grain-surface chemistry, particularly in this case involving deuterated ammonia, a naive extrapolation from the surface-chemistry involving H, D, C and O and a high grain-surface D/H ratio might explain the significant enhancement of deuterated ammonia (Caselli et al. 2004). However, the efficacy of this model is strongly dependent on the gas-phase atomic D/H ratio, which in the extreme case of our sample implies an enhancement of $\approx 10^4$ over the cosmic D/H ratio.

3.2.2. Comparison with deuteration in other star forming regions

Although the exact evolutionary status of the sources (i.e. pre/protostellar) in our sample cannot be determined with certainty, there are several observational evidences that substantiate their high mass pre/protostellar nature. The large line broadening ($1 < \Delta v < 5$ km s^{-1}) observed in all molecular tracers, together with the high H_2 column density ($N(H_2) > 10^{23}$ cm^{-2}) is characteristic of massive star forming regions. These sources have masses between a few hundred to a few thousand solar masses. Their source-averaged H_2 densities are a few 10^5 cm^{-3}– unlikely for low-mass objects. Moreover, the physical properties of these cores are similar to those associated with UCHII regions (e.g. Thompson et al. 2006). Therefore we expect them to be forming (or on the verge of forming) high-mass stars. The exact nature of these sources will be discussed in a future paper (Hatchell et al. in prep.).

The deuteration of a few tens of percent in ammonia is comparable to the highest which have been measured in the interstellar medium, which occur in low-mass prestellar cores. The related ratio $[N_2D^+]/[N_2H^+]$ exceeds 20% in a few prestellar cores including L1544 (Crapsi et al. 2004). High deuterated ammonia abundances have also been measured in early-stage protostars: the $[NH_2D]/[NH_3]$ ratio reaches over 30% in protostars in Perseus (Hatchell 2003), and detections of triply deuterated ammonia (van der Tak et al. 2002; Lis et al. 2002) and methanol (Parise et al. 2004) have all been in the environments of protostars, though deuteration of ∼5% is more common (Hatchell 2003; Saito et al. 2000; Shah & Wootten 2001). The high deuteration of our sample supports the idea that these are the high-mass equivalent of prestellar or protostellar cores.

Hot molecular cores, believed to be the early protostellar stage of high mass star formation and potentially a later evolutionary stage of our sources, have a low molecular deuteration fractionation $\sim 10^{-3}$, consistent with ice formation at a higher temperature of 60–80 K and little gas-phase deuteration, as expected at high temperatures (Hatchell et al. 1998, 1999; Roberts et al. 2002). High $[NH_2D]/[NH_3]$ ratios are observed in the Orion region but only in the compact ridge and not the hot core (Turner 1990). If our candidate precluster cores are precursors of hot cores, then the chemistry must radically alter during the later evolution of the hot core, perhaps with continuing accretion at higher temperatures during the early protostellar phase dominating the ice production.

3.3. Variations in HCN isotopic abundance

Let us define the abundance ratio, $R_{\rm iso}$, as

$$R_{\rm iso} = \frac{^{12}{\rm C}}{^{13}{\rm C}} \frac{^{15}{\rm N}}{^{14}{\rm N}}. \quad (7)$$

$R_{\rm iso}$ is found to vary with the distance from the Galactic center (Wilson & Rood 1994; Wielen & Wilson 1997). The observed trend can be explained by Galactic chemical evolution. Other observational studies (Ikeda et al. 2002; Langer & Penzias 1993; Dahmen et al. 1995) have found in addition a source-to-source variation of the isotopic ratios among a group of clouds located at nearly the same distance from the galactic centre.

The isotopomeric species of HCN, $H^{13}CN$ and $HC^{15}N$ have been often observed in their $J = 1$–0 transition toward various local molecular clouds (Dahmen et al. 1995; Hirota et al. 1998; Ikeda et al. 2002) to estimate the ratio $R_{\rm iso}$. These lines can be observed with the same receiver and hence the ratio derived will be independent of calibration errors. Moreover, the optical depth can be measured from the three hyperfine components of the $H^{13}CN$ line. As mentioned in Sect. 2.5, $H^{13}CN$ is optically thin in almost all cases and hence the observed ratios must indicate the abundance ratio $R_{\rm iso}$, since the column density estimates are free from bias due to photon trapping effects.

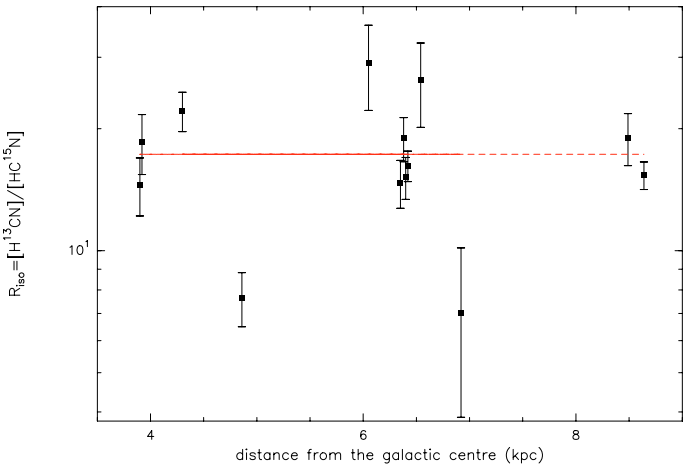

Fig. 6. $H^{13}CN$ and $HC^{15}N$ abundance ratio as a function of the distance from the galactic centre. The results are consistent with a single value of $R_{\rm iso} = 17$ shown as the dashed line.

In Fig. 6 we plot the abundance ratio of $H^{13}CN$ and $HC^{15}N$ as a function of distance from the galactic centre for our sources. The ratio of the abundances does not seem to correlate with the distance. However, the formal error bars are too large to be able to make any strong argument against a correlation of $R_{\rm iso}$ with galactocentric distance.

If we adopt the canonical values for the $^{12}C/^{13}C$ of 77 and $^{14}N/^{15}N$ of 450 toward the local interstellar medium (ISM), then the implied $H^{13}CN$ to $HC^{15}N$ abundance ratio is ∼6 (Wilson & Rood 1994, their Table 4). From our data, we find that most of the values tend to be higher, consistent with a mean value of 17. This ratio is intermediate between that found toward the galactic centre (∼30), an extreme high mass star-forming region and the local ISM (∼6) where typically low mass star formation pervades (see again Table 4 of Wilson & Rood 1994).

The SCAMPS sources are in the close vicinity of massive star forming regions and hence the energetic UV radiation could cause a isotope-selective photo-destruction (Schilke et al. 1992). Chemical fractionation is also likely to play an important role in the observed high values. The high deuterium fractionation we observed must be equally affecting the abundances of $H^{13}CN$ and $HC^{15}N$. Therefore, if at all, chemical fractionation were to play a role, it must be attributed to an anomalous fractionation in the isotopes of either N or C. A high ratio implies either a low ^{15}N fractionation or ^{13}C fractionation in HCN. As noted earlier in this section, the carbon isotopic ratio is known to vary across the Galaxy (Wilson & Rood 1994). The ratio is influenced mainly by a) the self-shielding property of CO, b)^{13}CO selective isotopic fractionation, and c) stellar winds from stars more massive than the sun, which favours the production of ^{13}C over ^{12}C (Krügel 2003). The deviation from the canonical value in the local ISM could be therefore due to a complex chemistry or environment in these high-mass star forming regions.

Although the number of assumptions involved is considerable, in particular that the two species may not be exactly tracing the same volume of gas as evidenced by the differences in their

line widths, the ratio we derive clearly indicates the differences in the properties of high mass and low mass star forming regions.

4. Conclusion

In this paper, we report the study of physical and chemical properties of a new sample of high-mass pre/protocluster clumps. We have observed 32 sources in the NH_3(1, 1) and (2, 2), NH_2D (1_{11}–1_{01}), $C^{18}O$(J = 1–0 and 2–1), $H^{13}CN$ and $HC^{15}N$ (J = 1–0) transitions. We have clear detections of NH_2D in 22 sources and 100% detection in NH_3.

Our observations suggest large deuterium enhancements (up to 66%), the largest reported so far. We also derived the amount of molecular depletion by comparing the $C^{18}O$ column density with the H_2 column density derived from dust continuum observations, and we find that the degree of CO depletion is a factor 2–12 higher compared to the canonical value for its abundance. The derived abundance ratio of $H^{13}CN$ to $HC^{15}N$ is indicative of a very high $^{13}C/^{12}C$ ratio, discrepant from that found toward the local ISM. These properties clearly reflect the complex chemistry in regions of high mass star formation.

This study shows that depletion and high deuteration exist towards massive cold cores in massive star forming regions and makes them promising candidates for the early phases of massive star formation. In a subsequent paper, we will discuss the spatial distribution of NH_2D in two sources observed with high angular resolution, confirming the high deuteration found from this study.

Acknowledgements. T. Pillai was supported for this research through a stipend from the International Max Planck Research School (IMPRS) for Radio and Infrared Astronomy at the University of Bonn. JH was supported at MPIfR Bonn by DFG SFB 494 and holds a PPARC AF at Exeter.

References

Bachiller, R., Guilloteau, S., & Kahane, C. 1987, A&A, 173, 324
Bacmann, A., Lefloch, B., Ceccarelli, C., et al. 2002, A&A, 389, L6
Bacmann, A., Lefloch, B., Ceccarelli, C., et al. 2003, ApJ, 585, L55
Bergin, E. A., & Langer, W. D. 1997, ApJ, 486, 316
Beuther, H., & Shepherd, D. 2005, ArXiv Astrophysics e-prints
Brown, P. D., & Millar, T. J. 1989a, MNRAS, 240, 25P
Brown, P. D., & Millar, T. J. 1989b, MNRAS, 237, 661
Carey, S. J., Clark, F. O., Egan, M. P., et al. 1998, ApJ, 508, 721
Caselli, P., Walmsley, C. M., Tafalla, M., Dore, L., & Myers, P. C. 1999, ApJ, 523, L165
Caselli, P., van der Tak, F. F. S., Ceccarelli, C., & Bacmann, A. 2003, A&A, 403, L37
Caselli, P., Stantcheva, T., & Herbst, E. 2004, in The Dense Interstellar Medium in Galaxies, ed. S. Pfalzner, C. Kramer, C. Staubmeier, & A. Heithausen, 479
Cesaroni, R., Churchwell, E., Hofner, P., Walmsley, C. M., & Kurtz, S. 1994, A&A, 288, 903
Cesaroni, R., Hofner, P., Walmsley, C. M., & Churchwell, E. 1998, A&A, 331, 709
Codella, C., Lorenzani, A., Gallego, A. T., Cesaroni, R., & Moscadelli, L. 2004, A&A, 417, 615
Crapsi, A., Caselli, P., Walmsley, C. M., et al. 2004, A&A, 420, 957
Crapsi, A., Caselli, P., Walmsley, C. M., et al. 2005, ApJ, 619, 379
Dahmen, G., Wilson, T. L., & Matteucci, F. 1995, A&A, 295, 194
Draine, B. T., & Lee, H. M. 1984, ApJ, 285, 89
Flower, D. R., Pineau Des Forêts, G., & Walmsley, C. M. 2005, A&A, 436, 933
Forveille, T., Guilloteau, S., & Lucas, R. 1989, Grenoble: IRAM
Frerking, M. A., Langer, W. D., & Wilson, R. W. 1982, ApJ, 262, 590
Hatchell, J. 2003, A&A, 403, L25
Hatchell, J., Millar, T. J., & Rodgers, S. D. 1998, A&A, 332, 695
Hatchell, J., Roberts, H., & Millar, T. J. 1999, A&A, 346, 227
Hirota, T., Yamamoto, S., Mikami, H., & Ohishi, M. 1998, ApJ, 503, 717
Ho, P. T. P., & Townes, C. H. 1983, ARA&A, 21, 239
Ikeda, M., Hirota, T., & Yamamoto, S. 2002, ApJ, 575, 250
Kramer, C., Alves, J., Lada, C. J., et al. 1999, A&A, 342, 257
Krügel, E. 2003, The physics of interstellar dust IoP Series in astronomy and astrophysics (Bristol, UK: The Institute of Physics)
Krügel, E., & Siebenmorgen, R. 1994, A&A, 288, 929
Langer, W. D., & Penzias, A. A. 1993, ApJ, 408, 539
Launhardt, R. 1996, Ph.D. Thesis
Lis, D. C., Roueff, E., Gerin, M., et al. 2002, ApJ, 571, L55
Menten, K. M., Pillai, T., & Wyrowski, F. 2005, in IAU Symp., 23
Millar, T. J. 2002, Planet. Space Sci., 50, 1189
Millar, T. J. 2003, Space Sci. Rev., 106, 73
Müller, H. S. P., Schlöder, F., Stutzki, J., & Winnewisser, G. 2005, J. Molec. Structure, 742, 215
Öberg, K. I., van Broekhuizen, F., Fraser, H. J., et al. 2005, ApJ, 621, L33
Ossenkopf, V., & Henning, T. 1994, A&A, 291, 943
Parise, B., Castets, A., Herbst, E., et al. 2004, A&A, 416, 159
Pickett, H. M., Poynter, R. L., Cohen, E. A., et al. 1998, J. Quant. Spectrosc. Radiat. Transf., 60, 883
Pillai, T., Wyrowski, F., Carey, S. J., & Menten, K. M. 2006, A&A, 450, 569
Roberts, H., & Millar, T. J. 2000a, A&A, 364, 780
Roberts, H., & Millar, T. J. 2000b, A&A, 361, 388
Roberts, H., Fuller, G. A., Millar, T. J., Hatchell, J., & Buckle, J. V. 2002, A&A, 381, 1026
Roberts, H., Herbst, E., & Millar, T. J. 2003, ApJ, 591, L41
Rodgers, S. D., & Charnley, S. B. 2001, ApJ, 553, 613
Roueff, E., Lis, D. C., van der Tak, F. F. S., Gerin, M., & Goldsmith, P. F. 2005, A&A, 438, 585
Saito, S., Ozeki, H., Ohishi, M., & Yamamoto, S. 2000, ApJ, 535, 227
Savage, B. D., & Mathis, J. S. 1979, ARA&A, 17, 73
Savva, D., Little, L. T., Phillips, R. R., & Gibb, A. G. 2003, MNRAS, 343, 259
Schilke, P., Walmsley, C. M., Pineau Des Forets, G., et al. 1992, A&A, 256, 595
Shah, R. Y., & Wootten, A. 2001, ApJ, 554, 933
Tafalla, M., Myers, P. C., Caselli, P., & Walmsley, C. M. 2004, A&A, 416, 191
Tafalla, M., Myers, P. C., Caselli, P., Walmsley, C. M., & Comito, C. 2002, ApJ, 569, 815
Tafalla, M., & Santiago, J. 2004, A&A, 414, L53
Thompson, M. A., Gibb, A. G., Hatchell, J. H., Wyrowski, F., & Pillai, T. 2005, in The Dusty and Molecular Universe: A Prelude to Herschel and ALMA, 425
Thompson, M. A., Hatchell, J., Walsh, A. J., MacDonald, G. H., & Millar, T. J. 2006, A&A, 453, 1003
Turner, B. E. 1990, ApJ, 362, L29
van der Tak, F. F. S., Schilke, P., Müller, H. S. P., et al. 2002, A&A, 388, L53
Walmsley, C. M., & Ungerechts, H. 1983, A&A, 122, 164
Watson, W. D. 1976, Rev. Mod. Phys., 48, 513
Wielen, R., & Wilson, T. L. 1997, A&A, 326, 139
Wilson, T. L., & Rood, R. 1994, ARA&A, 32, 191
Wood, D. O. S., & Churchwell, E. 1989, ApJS, 69, 831
Wu, L. X., & Yang, J. 2005, Acta Astron. Sinica, 46, 136

Online Material

Appendix A: Radiative transfer equations used for column density determination

We used the following expressions to determine the column density of the different molecules. The column density is given by,

$$N_{\rm tot} = \frac{3h\varepsilon_0}{2\pi^2 S\mu_g^2} J(T_{\rm ex}) Q(T_{\rm ex}) \tau \Delta v, \quad \text{(A.1)}$$

where, Δv is the linewidth, ε_0 is the dielectric permittivity, $S\mu_g^2$ is the line strength multiplied by the dipole moment along the molecular g-axis, τ is the optical depth, h is the Planck constant, $T_{\rm ex}$ is the excitation temperature and $Q(T_{\rm ex})$ is the partition function.

Here, $J(T_{\rm ex})$ is defined as

$$J(T_{\rm ex}) = \frac{\exp(E_{\rm u}/kT_{\rm ex})}{\exp(h\nu/kT_{\rm ex}) - 1}, \quad \text{(A.2)}$$

where $E_{\rm u}$ is the upper energy level, k is the Boltzmann constant and ν is the frequency of observed transition. We assume that the excitation temperature is the same for all rotational levels. Equation (A.1) is valid for the optically thick case.

In the optically thin case,

$$N_{\rm tot} = \frac{3h\varepsilon_0}{2\pi^2 S\mu_g^2} \frac{J(T_{\rm ex}) Q(T_{\rm ex}) W}{J_\nu(T_{\rm ex}) - J_\nu(2.7)}, \quad \text{(A.3)}$$

where W is the integrated intensity and $J_\nu(T)$ is defined as $J_\nu(T) = \frac{h\nu/k}{\exp(h\nu/kT_{\rm ex})-1}$.

The NH_2D partition function is determined by considering the contribution of the different energy levels from $J = 0$ to $J = 2$, while the metastable levels from $(J, K = 1, 1)$ to $(J, K = 3, 3)$ have been considered for NH_3.

For other molecular species, the partition function $Q(T_{\rm ex})$ at temperature $T_{\rm ex}$ is estimated as $Q(T_{\rm ex}) = \alpha T^\beta$, where α and β are the best fit parameters from a fit to the partition function obtained from JPL catalogue at different excitation temperatures from 10–300 K.

In Table A.1, we give the dipole moments we used for different molecules and the partition function, $Q(T_{\rm ex})$ at temperature $T_{\rm ex} = 15$ K.

By fitting the main and the hyperfine components of the (1, 1) line and the main component of the (2, 2) line, we obtain the rotational temperature. The kinetic temperature and NH_3 column density, have been derived using the standard formulation for NH_3 spectra (Bachiller et al. 1987). The NH_3 column density has been estimated assuming that the level populations are thermalised, i.e., $T_{\rm ex} = T_{\rm rot}$. A similar assumption holds for our estimation of NH_2D column densities.

The upper limit on the NHD_2 column density is estimated from the integrated intensity. This quantity was measured by integrating over a velocity range determined from the NH_2D line width around the LSR velocity of the source. The 1σ uncertainty on this value is estimated from the rms of the noise in the channels where no line emission is expected, and, is given by $\sqrt{N} v_{\rm res} \sigma$.

Table A.1. Molecular parameters used to estimate $N_{\rm tot}$.

Transition	$S\mu_g^{2a}$ D	$Q(15)^b$
NH_2D 1_{11}–1_{01} (para)	11.9	47.8[c]
NHD_2 1_{10}–1_{01} (ortho)	0.722	50.2[d]
$H^{13}CN$ $J = 1$–0, $F = 2$–1	14.84	22.8[e]
$HC^{15}N$ $J = 1$–0	8.909	7.6[e]
$C^{18}O$ $J = 1$–0	0.012	6.1[e]
$C^{18}O$ $J = 2$–1	0.024	6.1[e]

[a] S is the line strength and μ_g is the dipole moment along the molecular g-axis. [b] the partition function corresponding to a temperature of 15 K, the typical temperature of the sources in the present sample. [c] the partition function obtained by the summation over the contribution of the different energy levels from $J = 0$ to $J = 2$. [d] the partition function based on data from the CDMS catalog (Müller et al. 2005). [e] the partition function based on data from the JPL catalog (Pickett et al. 1998).

Table A.2. NH_3 line parameters with uncertainties (in brackets) from the hyperfine/Gaussian fits.

	NH_3 (1, 1)			NH_3 (2, 2)
Source	T_{MB} [a]	Δv [b]	τ_{mg} [c]	T_{MB}
	(K)	km s^{-1}		(K)
G8.13+0.25	1.9 (0.4)	1.5 (0.1)	1.5 (0.3)	1.0 (0.2)
	2.4 (0.4)	1.3 (0.1)	1.9 (0.3)	1.3 (0.2)
G8.68-0.37	5.3 (0.5)	1.1 (0.0)	5.0 (0.4)	2.3 (0.3)
	5.9 (0.4)	3.0 (0.1)	2.6 (0.1)	3.5 (0.2)
G8.71-0.37	3.5 (0.4)	1.3 (0.0)	4.2 (0.3)	1.7 (0.2)
G10.15-0.34	1.1 (0.1)	4.1 (0.3)	1.1 (0.5)	0.7 (0.1)
G10.21-0.31	2.9 (0.4)	1.9 (0.0)	3.9 (0.3)	1.8 (0.1)
G10.21-0.32	3.4 (0.5)	1.7 (0.0)	3.5 (0.2)	1.8 (0.3)
	4.6 (0.4)	1.9 (0.0)	4.6 (0.2)	2.7 (0.1)
G10.61-0.33	2.0 (0.2)	1.9 (0.1)	1.8 (0.3)	1.1 (0.1)
G11.11-0.12P1	5.1 (1.0)	1.3 (0.1)	3.5 (0.4)	1.9 (0.3)
G11.11-0.12P3	3.0 (2.2)	2.5 (0.1)	2.4 (0.2)	1.0 (0.2)
G11.11-0.12P4	4.3 (0.9)	1.5 (0.1)	3.1 (0.6)	0.9 (0.4)
G12.19-0.12	0.4 (0.0)	3.9 (0.2)	1.8 (0.3)	0.1 (0.0)
G13.18+0.06	5.4 (0.5)	2.4 (0.0)	3.3 (0.1)	3.7 (0.1)
G15.01-0.67	5.0 (0.4)	2.9 (0.1)	0.7 (0.1)	3.6 (0.1)
G15.01-0.69	3.3 (0.2)	2.6 (0.1)	0.5 (0.1)	2.3 (0.1)
G15.03-0.65	2.6 (0.3)	2.4 (0.2)	1.2 (0.3)	1.6 (0.2)
	2.8 (0.3)	2.6 (0.1)	1.3 (0.3)	1.2 (0.4)
G18.17-0.30	2.9 (0.3)	1.6 (0.0)	3.3 (0.2)	1.7 (0.1)
G18.21-0.34	3.8 (0.4)	1.5 (0.0)	2.8 (0.2)	2.0 (0.2)
G19.30+0.07P1	5.0 (0.7)	2.0 (0.1)	2.1 (0.3)	2.7 (0.2)
G19.30+0.07P2	3.2 (0.6)	1.7 (0.1)	2.9 (0.5)	1.4 (0.3)
G23.41-0.23	3.0 (0.3)	2.0 (0.1)	1.2 (0.1)	1.6 (0.2)
G23.42-0.23	2.2 (0.3)	1.9 (0.1)	1.6 (0.2)	1.3 (0.1)
	1.3 (0.4)	1.5 (0.1)	0.6 (0.4)	0.4 (0.1)
G23.44-0.18	3.6 (0.2)	3.6 (0.1)	1.7 (0.1)	2.8 (0.1)
G27.29+0.15	1.7 (0.2)	2.5 (0.1)	1.6 (0.2)	0.9 (0.1)
G27.31+0.18	1.0 (0.2)	2.1 (0.1)	2.1 (0.4)	0.6 (0.1)
G28.34+0.06P1	2.7 (0.5)	2.7 (0.0)	2.0 (0.1)	1.3 (0.1)
G28.34+0.06P2	2.8 (0.5)	2.0 (0.1)	2.7 (0.3)	1.5 (0.2)
G29.97-0.05	0.8 (0.2)	2.0 (0.0)	2.4 (0.2)	0.3 (0.0)
G33.71-0.01	2.0 (0.4)	2.4 (0.2)	2.9 (0.6)	1.5 (0.2)
G34.81-0.28	4.7 (0.5)	1.4 (0.0)	1.6 (0.2)	2.2 (0.1)
G35.19-1.73	4.7 (0.4)	1.6 (0.0)	1.8 (0.1)	2.4 (0.1)
G79.34+0.33	2.4 (0.3)	1.2 (0.0)	1.5 (0.1)	0.7 (0.1)
G81.74+0.59	6.1 (0.6)	2.2 (0.0)	1.3 (0.1)	3.2 (0.1)

[a] Main beam brightness temperature from gaussian fit. [b] *FWHM* from the hyperfine fits. [c] optical depth of the main group of hyperfines from the hyperfine fits.

Note: Five sources clearly have at least 2 velocity components, hence the fit parameters have been determined for each component. Similar notations are used for other molecules elsewhere in this paper. The parameter has been fixed for the fit for those entries with no error indicated.

Table A.3. NH_2D line parameters with uncertainties (in brackets) from the hyperfine/Gaussian fits.

	NH_2D 85.93 GHz		
Source	$\int T_{MB} dv^a$	Δv^b	$\tau_{tot}{}^c$
	K km s^{-1}	km s^{-1}	
G8.13+0.25	0.5 (<0.1)	1.3 (0.3)	–
	0.7 (<0.1)	1.8 (0.9)	–
G8.68-0.37	–	1.2 (0.1)	2.2 (0.7)
G8.71-0.37	–	1.1 (<0.1)	3.7 (0.6)
G10.21-0.31	–	1.2 (0.1)	3.4 (1.4)
G10.21-0.32	–	1.4 (0.1)	2.3 (1.0)
G10.61-0.33	0.3 (<0.1)	1.5 (0.2)	–
G11.11-0.12P1	–	1.0 (0.1)	3.6 (1.5)
G11.11-0.12P4	0.4 (0.1)	1.3 (0.2)	–
G12.19-0.12	1.5 (0.1)	3.6 (0.5)	–
G13.18+0.06	–	2.2 (0.1)	2.0 (0.5)
G18.17-0.30	–	1.5 (0.1)	4.4 (1.1)
G18.21-0.34	–	1.3 (0.1)	2.0 (0.8)
G23.41-0.23	–	1.7 (0.2)	2.1 (1.3)
G23.44-0.18	1.4 (0.1)	3.1 (0.2)	–
G27.29+0.15	0.4 (0.1)	1.5 (0.4)	–
G28.34+0.06P2	1.2 (0.1)	1.8 (0.2)	–
G29.97-0.05	–	1.4 (0.1)	3.0 (0.6)
G33.71-0.01	0.4 (<0.1)	1.6 (0.3)	–
G34.81-0.28	0.8 (0.1)	1.7 (0.1)	–
G35.19-1.73	–	1.4 (<0.1)	2.7 (0.4)
G79.34+0.33	–	1.0 (0.9)	1.1 (0.1)
G81.74+0.59	–	2.8 (0.1)	1.5 (0.3)

[a] Integrated intensity of the line from the Gaussian fits. [b] *FWHM* from the hyperfine fits. [c] Total optical depth from the hyperfine fits.
Note: Similar notations are used for other molecules elsewhere in this paper. The parameter has been fixed for the fit for those entries with no error indicated.

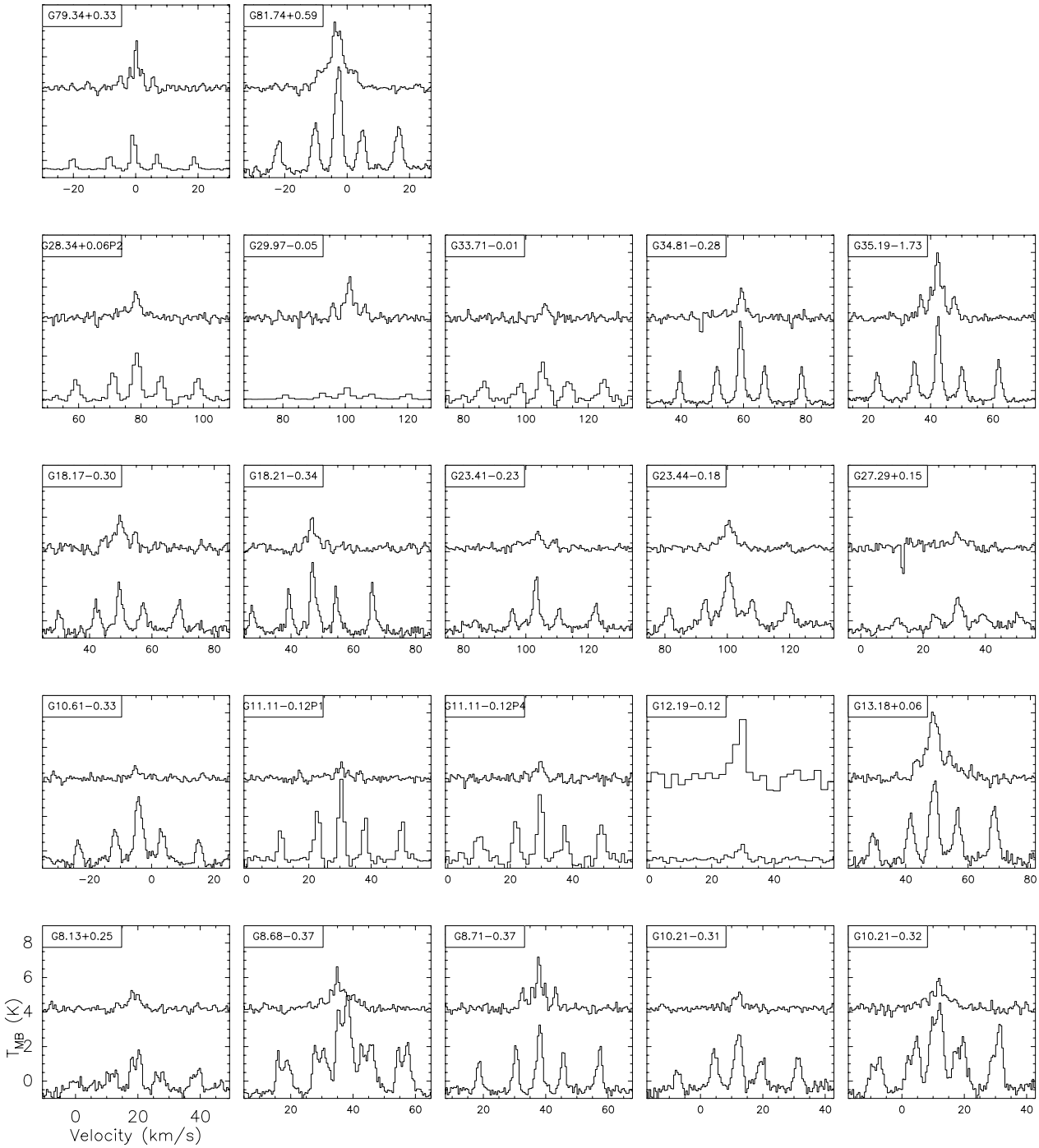

Fig. A.1. *Lower spectrum in each panel*: Effelsberg 100 m observation of the NH_3 (1, 1) emission. *Upper spectrum in each panel*: 30 m observation of the NH_2D at 85.9 GHz. The NH_2D is scaled by a factor 5.0 to amplify the emission relative to NH_3 in the absolute (brightness temperature) units.

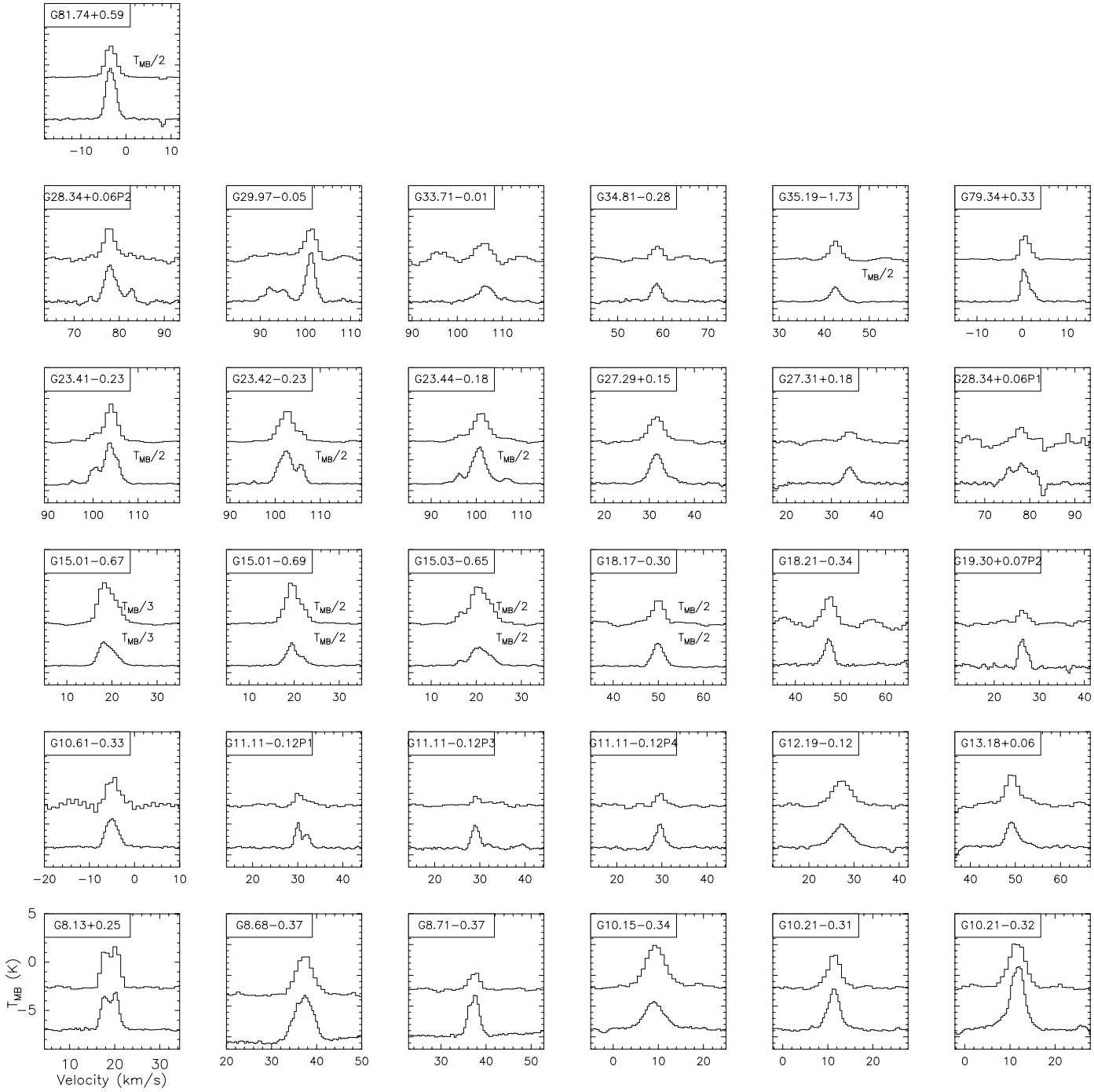

Fig. A.2. *Lower spectrum*: 30 m $C^{18}O$ (J = 1–0). *Upper spectrum*: 30 m $C^{18}O$ (J = 2–1). The velocity range is ±15 km s^{-1} of the systemic velocity.

Table A.4. $C^{18}O$ (J = 1–0) and (J = 2–1) line parameters.

Source	$C^{18}O$ (J = 1–0) $\int T_{MB} dv$	$C^{18}O$ (J = 2–1) $\int T_{MB} dv$
	K km s^{-1}	K km s^{-1}
G8.13+0.25	15.7 (0.1)	27.6 (0.5)
G8.68-0.37	24.9 (0.9)	31.9 (1.7)
G8.71-0.37	13.5 (0.4)	5.9 (0.7)
G10.15-0.34	15.6 (0.3)	37.4 (0.5)
G10.21-0.31	14.9 (0.2)	19.0 (0.4)
G10.21-0.32	27.5 (0.3)	33.2 (0.6)
G10.61-0.33	10.6 (0.3)	14.7 (0.5)
G11.11-0.12P1	6.1 (0.1)	5.5 (0.4)
G11.11-0.12P3	5.1 (0.3)	5.1 (0.5)
G11.11-0.12P4	5.1 (0.2)	4.8 (0.5)
G12.19-0.12	12.0 (0.2)	20.8 (0.4)
G13.18+0.06	9.7 (0.5)	20.9 (0.8)
G15.01-0.67	31.0 (0.2)	91.7 (1.0)
G15.01-0.69	16.2 (0.2)	53.7 (0.5)
G15.03-0.65	19.8 (0.2)	65.5 (0.6)
G18.17-0.30	13.1 (0.7)	26.5 (1.3)
G18.21-0.34	7.3 (0.4)	12.0 (1.3)
G19.30+0.07P1[a]	1.1 (0.4)	–
G19.30+0.07P2	4.1 (0.4)	6.6 (0.7)
G23.41-0.23	35.2 (0.8)	44.5 (1.0)
G23.42-0.23	31.5 (0.3)	43.1 (0.5)
G23.44-0.18	31.1 (0.5)	43.4 (0.6)
G27.29+0.15	12.4 (0.2)	16.6 (0.5)
G27.31+0.18	4.9 (0.2)	6.1 (0.5)
G28.34+0.06P1	11.3 (0.4)	6.3 (1.5)
G28.34+0.06P2	14.4 (0.5)	19.1 (0.7)
G29.97-0.05	12.9 (0.7)	18.2 (0.9)
G33.71-0.01	7.4 (0.2)	9.0 (1.3)
G34.81-0.28	5.4 (0.3)	6.6 (0.6)
G35.19-1.73	8.4 (0.2)	15.8 (0.8)
G79.34+0.33	7.8 (0.1)	9.9 (0.2)
G81.74+0.59	14.9 (0.2)	32.4 (0.4)

$\int T_{MB} dv$ is the integrated intensity over ±5 km s^{-1}of the brightest $C^{18}O$ (J = 1–0) peak. [a] $C^{18}O$ (J = 2–1) data suffered from baseline ripples.

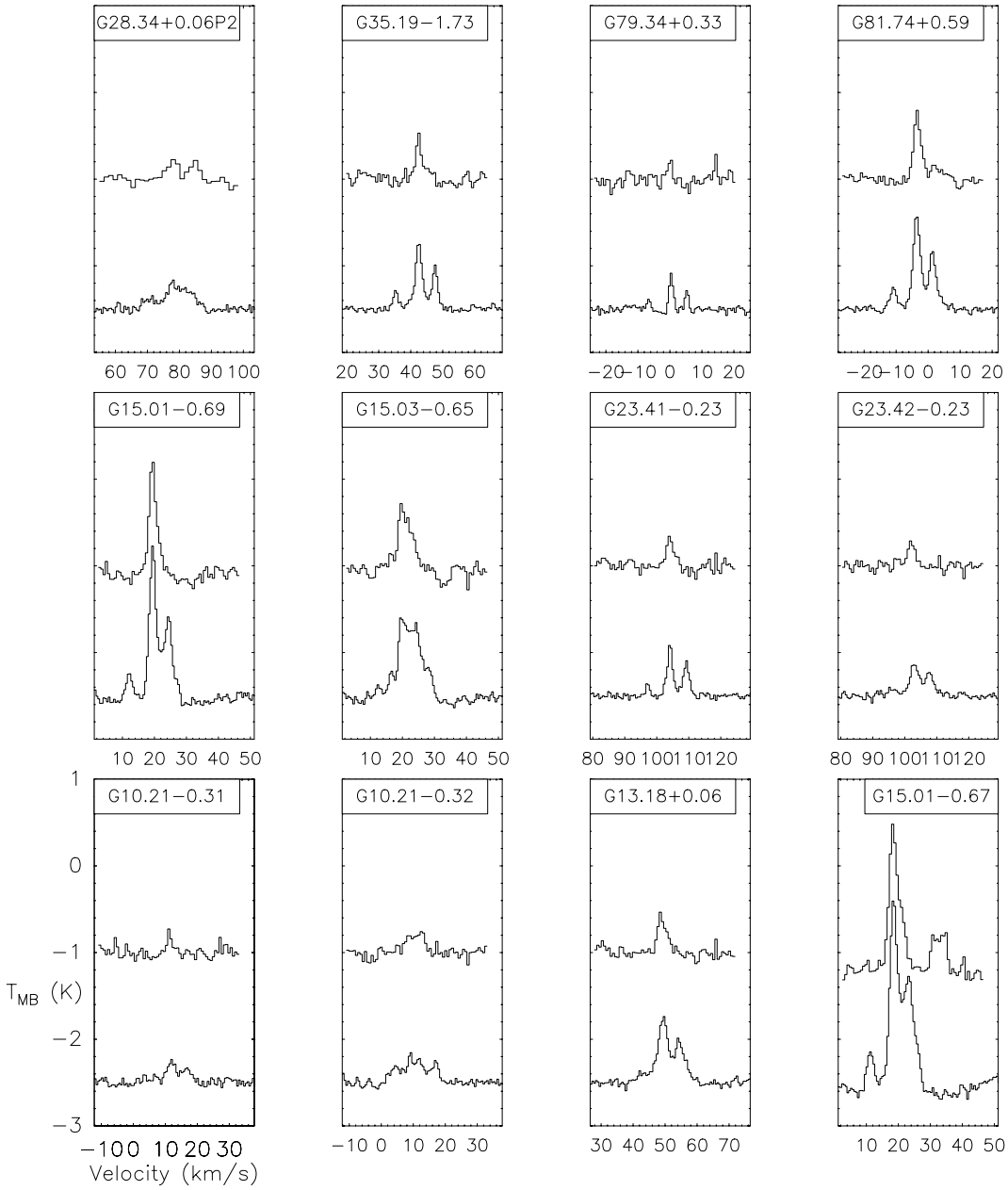

Fig. A.3. *Lower spectrum*: 30 m observation of $H^{13}CN$. *Upper spectrum*: 30 m observation of $HC^{15}N$. The $HC^{15}N$ is scaled by a factor 2 to amplify the emission relative to $H^{13}CN$ in the absolute units. The velocity range is ±25 km s^{-1} of the systemic velocity.